Transverse Resolution in Through-the-Wall Radar Imaging

Maria Antonia Maisto, Mehdi Masoodi, and Raffaele Solimene

Abstract – In this article, the estimation of transverse resolution in a typical through-the-wall radar imaging scenario under a linearized scattering approximation is addressed. The geometry is scalar and two-dimensional, and the data are collected at a single frequency with a monostatic configuration. The measurement domain is located near the no-reactive zone, so that the evanescent contribution can be neglected, and the resolution is limited mainly to the configuration parameters. In particular, we succeed in estimating a closed formula that highlights the role of the configuration parameters on the achievable resolution.

1. Introduction

The electromagnetic wave capability to "see" through obstacles, such as walls, doors, and other visually opaque materials, is considered a powerful tool for a variety of applications, both military and civilian. Through-the-wall radar imaging (TWRI) needs to solve an electromagnetic inverse scattering problem within a nonhomogeneous scattering scenario representing the wall [1–3]. As is well known, such a problem is nonlinear and ill-posed. However, if quantitative reconstructions are not required, the problem can be linearized, for example, using the Born approximation. Accordingly, this article considers the TWRI problem under a linearized scattering approximation. The ill-posedness can be addressed by introducing some regularization procedures [4]. However, they lead to a trade-off between accuracy and stability, limiting the achievable resolution. In this framework, determining the achievable resolution and how it depends on the configuration parameters is of great importance since, having set the configuration, one can foresee the achievable performance during the imaging stage, or, vice versa, given the resolution, the configuration can be settled accordingly [5–7]. The aim of this article is to find an analytical estimation of the transverse resolution for a through-the-wall scenario and how it is affected by configuration parameters. Since the framework is linear, the resolution can be estimated as the main lobe width of the point-spread function (psf), defined as the impulsive response of the system composed of the cascade of the forward operator and its regularized inverse. The psf shows how the point scatterer spreads because of the filtering process introduced by the inversion scheme. In general, the psf (and hence resolution) can depend on the imaging algorithm (or, equivalently, on the adopted regularization scheme). However, it can be shown that if no a priori information concerning the sparsity on the unknown solution [8–10] is exploited, different regularization schemes introduce a similar filtering on the unknown solution. While for data collected in the far field the psf is a band-limited function that results in a spatially invariant filtering, in the near field, this is not true. However, it can be shown that if the wall thickness and the distance between the investigation and the measurement domains is sufficiently large, the evanescent wave contribution can be neglected, and the psf can be expressed as a function with a spatially varying band [5–7]. This results in a spatially varying filtering on the unknown solution that implies a nonuniform behavior of the resolution. In particular, we succeed in reexpressing the psf as a band-limited function with respect to a proper "warping" variable [5–7] whose dependence on the starting variable is nonlinear. Accordingly, the uniform main beam width of the psf in the warping variable becomes nonuniform in the starting variable. Finally, the achievable transverse resolution for TWRI is compared to the ones obtainable for subsurface and homogeneous scenarios. This article can be considered a companion of [11], where the focus was on determining a sampling strategy for collecting a scattered field.

2. Scattering Model

Consider the classical TWRI scenario sketched in Figure 1, where the wall is schematized as a three-layer medium (air-wall-air) with L and ε_r the wall thickness and permittivity. Invariance occurs along the y-axis, so the problem is scalar and two-dimensional. The investigation domain is a strip $SD = [-X_s, X_s]$ parallel to the x-axis, located at the depth z and embedded within the third layer. Data are collected at a single frequency with a monostatic configuration where the transmitting and receiving antenna move together along the segment $OD = [-X_o, X_o]$ placed at z_o in the first layer. Under the Born approximation, the scattered field E_s is given by

$$E_s(x_o) = jk_0^2\omega\mu_0 \int_{SD} G^2(x_o, x)\chi(x)dx \qquad (1)$$

with k_0 the free space wavenumber. Equation (1) in operator notation is written as

$$\mathcal{A} : \chi \in L^2(SD) \to E \in L^2(OD) \qquad (2)$$

Manuscript received 9 August 2022.

M. A. Maisto, M. Masoodi, and R. Solimene are with the Diparitmento di Ingegneria, Universitá degli Studi della Campania, Luigi Vanvitelli, 81031 Aversa, Italy; e-mail: mariaantonia.maisto@unicampania.it.

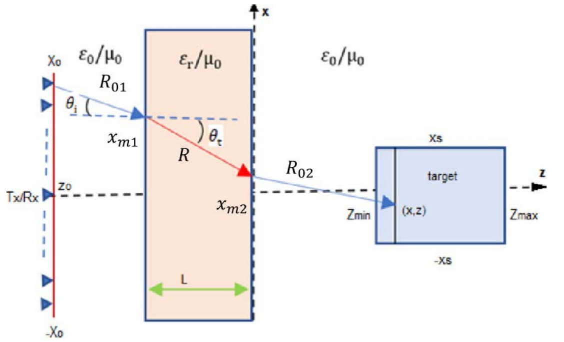

Figure 1. Geometry of the problem.

The function $\chi(x) = (\varepsilon_s(x) - \varepsilon_0)/\varepsilon_0$ is the so-called contrast function, with ε_s being the dielectric permittivity of the unknown scatterer, representing the unknown solution of the problem. The function $G^2(x_o, x,)$ is the square of $G(x_o, x,)$, that is, the Green function accounting for a three-layered background medium whose spectral representation is reported in [2]. If it is assumed that $L > \frac{\lambda_0}{n}$ and $z - L - z_o > \lambda_0$, with λ_0 the free space wavelength and $n = \sqrt{\varepsilon_r}$ the refractive index, the exponential terms in the spectral representation of $G(x_o, x)$ are very oscillating terms, and hence the asymptotic evaluation of the integral can be applied, resulting in

$$G(x_o, x) \approx \sqrt{h(x_o, x)}e^{-jk_0\phi(x_o,x)} \tag{3}$$

where $\sqrt{h(x_o, x)}$ is the relevant amplitude factor and $\phi(x_o, x) = (R_{01} + R_{02} + nR)$ is the phase term that takes into account the three paths from the target point $\boldsymbol{r} = (x, z)$ to the field point $\boldsymbol{r}_o = (x_o, z_o)$, through which the waves propagate. In particular, $R_{01} = \sqrt{(x_{m1}(x_o, r) - x_o)^2 + (L + z_o)^2}$, $R_{02} = \sqrt{(x - x_{m2}(x_o, r))^2 + z^2}$ and $R = \sqrt{(x_{m2}(x_o, r) - x_{m1}(x_o, r))^2 + L^2}$ are the two paths traveled by the waves in free space and the one traveled by the waves in the wall, respectively. Finally, $x_{m1}(x_o, x)$ and $x_{m2}(x_o, x)$ are the refraction points, which are given by Snell's law as

$$\frac{x_{m1} - x_o}{R_{01}} = n\frac{x_{m2} - x_{m1}}{R} = \frac{x - x_{m2}}{R_{02}} \tag{4}$$

By adopting the classical Rayleigh criterion, the achievable resolution can be estimated as the distance between the maximum and the first zero of the psf of the imaging procedure. The latter represents the reconstruction of a point-like scatterer. Let $\{u_n, v_n, \sigma_n\}_{n=0}^{\infty}$ be the singular system of the scattering operator, with u_ns and v_ns spanning the domain of the operator $\mathcal{A}$ (Dom($\mathcal{A}$)) and the closure of its range ($\bar{R}(\mathcal{A})$), respectively. By exploiting as an inversion algorithm the truncated singular value decomposition [4], the psf can be formally expressed as

$$psf(x, x') = \sum_{n=0}^{N_\varepsilon} u_n(x')u_n(x) \tag{5}$$

Say that ε is the noise-dependent truncation level and that N_ε is the number of singular values above it. Equation (5) shows that the psf and hence the resolution can be in general noise dependent. In practice, the assumptions $L > \frac{\lambda_0}{n}$ and $z - L - z_o > \lambda_0$ imply that the evanescent contribution can be neglected. As a consequence, the singular values exhibit an abrupt exponential decay beyond a certain critical index, and it is natural to identify such an index as the so-called number of degrees of freedom of the problem. As a consequence, the psf turns out to be weakly dependent on the signal-to-noise ratio and the regularization scheme. Hence, the resolution depends mainly on the configuration parameters. Since (5) is not known in closed form, in the next section we look for an approximation of it.

3. Point-Spread Function Estimation

According to [5–7], we look for an approximation of (5) by exploiting the weighted adjoint method (WAM) as inversion scheme. The reconstruction can be written as

$$\chi_R(x) = (\mathcal{A}^{\dagger}W(x, x_o)\mathcal{A}\chi)(x) = \int_{-X_s}^{X_s} \chi(x')dx' \times$$

$$\int_{-X_0}^{X_0} W(x, x_o)h^*(x_o, x)h(x_o, x')e^{2j[\phi(x_o,x) - \phi(x_o,x')]}dx_o \tag{6}$$

where $W(x, x_o)$ is a weighting function. Such an inversion scheme differs from common adjoint-based methods because of $W(x, x_o)$, which makes such an inversion scheme a regularization in the sense of Tichhonov [4]. While in adjoint methods only the propagator phase is precisely compensated at the target position, in WAM the weighing function allows one to properly address also the amplitude term. In fact, W must be chosen so that the corresponding psf is as close as possible to a filtered version of a Dirac-delta function. By following the same steps developed in [7] and by choosing $W(x, x_o) = 2|\frac{\partial^2\phi(x_o,x)}{\partial x_o \partial x}|\frac{1}{|h(x_o,x)|^2}$, we arrive at the following psf estimation:

$$psf_W(\eta, \eta') = 2e^{jk_0(\gamma(\eta) - \gamma(\eta'))}sinc[k_0(\eta - \eta')] \tag{7}$$

where $\gamma(x) = [\phi(-X_0, x) + \phi(X_0, x)]$ and $\eta(x) = [\phi(-X_0, x) - \phi(X_0, x)]$

To make explicit the dependence of $\eta(x)$ in terms of x, we need to determine the two refraction points x_{m1} and x_{m2} by solving (4). This issue can be simplified by exploiting an equivalent two-layered model (see [2]). This allows one to reexpress the phase term in (3) as $\phi(x_o, x) = nR(x_o, x) + R_0(xo, x)$ with $R(x_o, x) = \sqrt{(x_{m3} - x_o)^2 + L^2}$ and $R_0(x_o, x) = \sqrt{(x - x_{m3})^2 + (z - L - z_o)^2}$ in terms of only one refraction point x_{m3} fulfilling

$$\frac{x - x_{m3}}{R_0} = n\frac{x_{m3} - x_o}{R} \tag{8}$$

By introducing this equivalent reformulation, the dependence of $\eta(x)$ in terms of x becomes

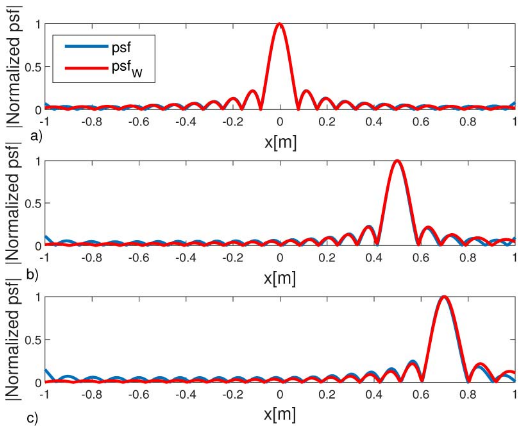

Figure 2. Normalized psf amplitudes for (a) $f = 1.2$ GHz, $n = 3$, $d = 0.25$ m, $z_o = -0.5$ m, $z = 0.5$ m, $X_o = 1$ m, $X_s = 1$ m, and $x' = 0$ m; (b) $x' = 0.5$ m; and (c) $x' = 0.7$ m. The blue lines refer to *psf*, whereas the red ones to *psf*$_W$.

$$\eta(x) = n$$

$$[n\sqrt{(X_0+f_1(x))^2+L^2}+\sqrt{(f_1(x)-x)^2+(z-L-z_o)^2}-$$

$$-n\sqrt{(X_0-f_2(x))^2+L^2}-\sqrt{(f_2(x)-x)^2+(z-L-z_o)^2}]$$

with $f_1(x) = x_{m3}(-X_0, x)$ and $f_2(x) = x_{m3}(X_0, x)$. By exploiting $f_1(-x) = -f_2(x)$, (9) can be rewritten as

$$\begin{aligned}\eta(x) = [&n\sqrt{(X_0+f_1(x))^2+L^2}\\ &+\sqrt{(f_1(x)-x)^2+(z-L-z_o)^2}-\\ &-n\sqrt{(X_0+f_1(-x))^2+L^2}\\ &-\sqrt{(f_1(-x)+x)^2+(z-L-z_o)^2}]\end{aligned} \tag{10}$$

This makes it clear that $\eta(x)$ is an odd function of x and, hence, $\eta(X_s) = -\eta(-X_s)$.

In order to ensure that *psf*$_W$ returned by (7) provides a good approximation of *psf*, some numerical examples are considered. The psf is obtained by numerically computing the singular system of $\mathcal{A}$ and by retaining in (5) the singular functions corresponding to the singular values preceding the abrupt decay. The simulations show an excellent agreement between *psf*$_W$ and *psf*. As a representative example, here we report the case shown in Figure 2. The parameters are $X_s = 1$ m, $z = 0.5$ m, $X_0 = 1$ m, $z_o = -0.5$ m, $L = 0.25$ m, $n = 3$, and $k_0 = 8\pi$ m^{-1}. Each panel of the figure shows *psf* (blue line) and *psf*$_W$ (red line) for different locations of the point-like scatterer: $x' = 0$ (a), $x' = 0.5$ (b), and $x' = 0.7$ (c). As can be appreciated, the two functions overlap very well; accordingly, it can be concluded that (7) works very well and can be used to estimate the achievable resolution.

4. Resolution Estimation

By applying Rayleigh's criterion, the resolution is estimated as the main lobe of *psf*$_W(\eta, \eta')$. By doing so, it is immediately seen that, in the η variable, the resolution is $\Delta\eta = \frac{\pi}{k_0}$, which, in terms of the x variable, is

$$\eta(x+\Delta x) - \eta(x) = \frac{\pi}{k_0} \tag{11}$$

It is evident that since the relationship between $\eta(x)$ and x is nonlinear, uniform resolution in η becomes nonuniform in x. This means that a target along the x-axis is not reconstructed with the same resolution. Such a spatially varying behavior is common in the near field, and it is already observed for other configurations, such as homogeneous and subsurface scenarios. However, here the dependence between $\eta(x)$ and x is affected by geometrical parameters in a different way. In particular, it is interesting to compare the resolution for three scenarios: the TWI scenario (Δx_{tw}), the subsurface scenario (Δx_{ss}), and the free space homogeneous scenario (Δx_h). For the subsurface scenario, the third layer in Figure 1 is assumed equal to the second one with relative permittivity ε_r. Also, in this case, we need to solve (11) for Δx, but the dependence of η in terms of x is different and given by

$$\begin{aligned}\eta_{ss}(x) = &\sqrt{(X_0+f_3(x))^2+(-z_o-L)^2}+\\ &+n\sqrt{(f_3(x)-x)^2+(z+L)^2}-\\ &-\sqrt{(X_0+f_3(-x))^2+(-z_o-L)^2}-\\ &-n\sqrt{(f_3(-x)+x)^2+(z+L)^2}\end{aligned} \tag{12}$$

with f_3 solving

$$\begin{aligned}&n\frac{x-f_3}{\sqrt{(f_3(x)-x)^2+(z+L)^2}}\\ &=\frac{f_3+X_0}{\sqrt{(X_0+f_3(x))^2+(-z_o-L)^2}}\end{aligned} \tag{13}$$

For the homogeneous scenario, η in terms of x is

$$\begin{aligned}\eta_h(x) = &\sqrt{(X_0+x)^2+(z-z_o)^2}\\ &-\sqrt{(X_0-x)^2+(z-z_o)^2}\end{aligned} \tag{14}$$

Figure 3 shows Δx_{tw}, Δx_{ss}, and Δx_h in terms of x for two values of X_0. The other parameters are set as in the example shown in Figure 2. As can be seen, for the all scenarios, resolution gets worse when x moves toward the edges of *SD*. However, as X_0 increases, it tends to become constant. Therefore, the nonuniform behavior of the resolution is essentially due to truncation effects. Moreover, having fixed the configuration parameters, Δx_{tw} is always lower than Δx_h but larger than Δx_{ss}. Accordingly, this entails that reconstructions can benefit from a priori information concerning the features of the nonhomogeneous scenario. In particular, this is especially true for the

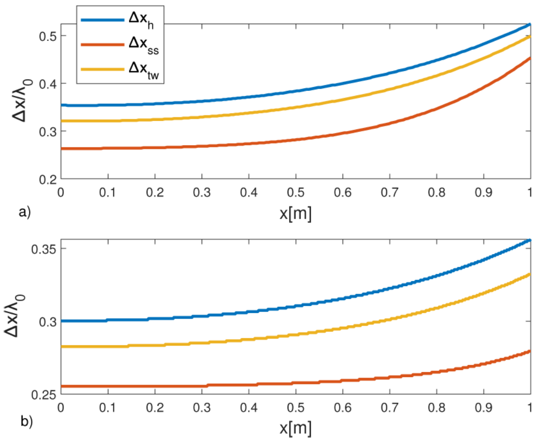

Figure 3. Δx_{tw} (yellow line), Δx_{ss} (red line), and Δx_h (blue line) normalized with respect to λ_0 is shown in terms of x for two values: (a) X_0: $X_0 = 1$ m and (b) $X_0 = 1.5$ m. Other parameters are the same as Figure 2.

subsurface case. In fact, as can be seen, Δx_{ss} at the center of *SD* reaches $\lambda_0/4$. This is the best resolution if evanescent waves are neglected.

5. Conclusion

In this article, the estimation of transverse resolution in a typical TWRI scenario has been addressed. In particular, a closed formula expression that highlights the role of the configuration parameters on the achievable resolution has been derived. Like the homogeneous and subsurface scenarios, the boundedness of observation domain X_0 introduces a spatially varying behavior, meaning that a target along the x-axis cannot be reconstructed with the same accuracy. However, the dependence of Δx_{tw}, Δx_{ss}, and Δx_h on the geometrical parameters is different. In fact, it is shown that Δx_{tw} is always lower than Δx_h but larger than Δx_{ss}. Accordingly, the reconstructions can benefit from a priori information concerning the nonhomogeneous scenario.

6. References

1. M. G. Amin, *Through-the-Wall Radar Imaging*, Boca Raton, FL, CRC Press, 2017.
2. M. A. Maisto, M. Masoodi, R. Pierri, and R. Solimene, “Sensor Arrangement in Through-the Wall Radar Imaging,” *IEEE Open Journal of Antennas and Propagation*, **3**, 2022, pp. 333-341.
3. A. Randazzo, C. Ponti, A. Fedeli, C. Estatico, P. D’Atanasio, et al., “A Two-Step Inverse-Scattering Technique in Variable-Exponent Lebesgue Spaces for Through-the-Wall Microwave Imaging: Experimental Results,” *IEEE Transactions on Geoscience and Remote Sensing*, **59**, 2021, pp. 7189-7200.
4. M. Bertero, “Linear Inverse and Ill-Posed Problems,” *Advances in Electronics and Electron Physics*, **75**, 1989, pp. 1-120.
5. M. A. Maisto, R. Solimene, and R. Pierri “Resolution limits in inverse source problem for strip currents not in Fresnel zone,” *Journal of the Optical Society of America A*, **36**, 5, 2019, pp. 826-833.
6. M. A. Maisto, R. Pierri, and R. Solimene, “Near-Field Transverse Resolution in Planar Source Reconstructions,” *IEEE Transactions on Antennas and Propagation*, **69**, 8, 2021, pp. 4836-4845.
7. M. A. Maisto, R. Solimene, and R. Pierri “Transverse Resolution in Microwave Imaging for Strip Objects Buried in a Half-Space Medium,” *Progress In Electromagnetics Research M*, **88**, 2020, pp. 145-157.
8. A. S. Barzegar, A. Cheldavi, S. H. Sedighy, and V. Nayyeri, “3-D Through-the-Wall Radar Imaging Using Compressed Sensing,” *IEEE Geoscience and Remote Sensing Letters*, **19**, 2022, pp. 1-5.
9. F. H. C. Tivive and A. Bouzerdoum, “Through the Wall Scene Reconstruction Using Low Rank and Total Variation,” *IEEE Transactions on Computational Imaging*, **6**, 2020, pp. 221-234.
10. Q. Guo, Y. Li, X. Liang, J. Dong, and R. Cheng, “A Novel CT-Mode Through-the-Wall Imaging Method Based on Time Delay Estimation,” *IEEE Geoscience and Remote Sensing Letters*, **18**, 2021, pp. 1381-1385
11. M. A. Maisto, M. Masoodi, and R. Solimene, “Spatial Sensor Arrangement in Through-the Wall Radar Imaging: Numerical Results,” 3rd URSI Atlantic and Asia Pacific Radio Science Meeting (AT-AP-RASC), Gran Canaria, Spain 29 May - 3 June, 2022, pp. 1-4.